

PdCu Nanoalloy Electrocatalysts in Oxygen Reduction Reaction: Role of Composition and Phase State in Catalytic Synergy

Jinfang Wu,^{†,‡} Shiyao Shan,[‡] Jin Luo,[‡] Pharrah Joseph,[‡] Valeri Petkov,[§] and Chuan-Jian Zhong^{*,‡}

[†]Department of Chemistry and Chemical Engineering, Chongqing University, Chongqing 400030, China

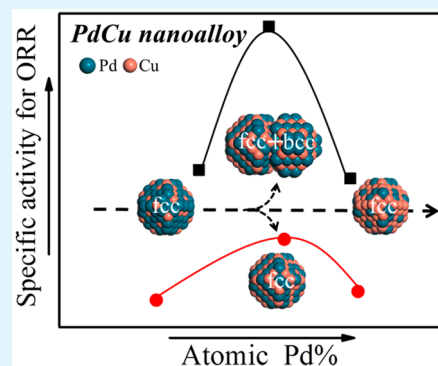
[‡]Department of Chemistry, State University of New York at Binghamton, Binghamton, New York 13902, United States

[§]Department of Physics, Central Michigan University, Mt. Pleasant, Michigan 48859, United States

Supporting Information

ABSTRACT: The catalytic synergy of nanoalloy catalysts depends on the nanoscale size, composition, phase state, and surface properties. This report describes findings of an investigation of their roles in the enhancement of electrocatalytic activity of PdCu alloy nanoparticle catalysts for oxygen reduction reaction (ORR). Pd_nCu_{100-n} nanoalloys with controlled composition and subtle differences in size and phase state were synthesized by two different wet chemical methods. Detailed electrochemical characterization was performed to determine the surface properties and the catalytic activities. The atomic-scale structures of these catalysts were also characterized by high-energy synchrotron X-ray diffraction coupled with atomic pair distribution function analysis. The electrocatalytic activity and stability were shown to depend on the size, composition, and phase structure. With Pd_nCu_{100-n} catalysts from both methods, a maximum ORR activity was revealed at Pd/Cu ratio close to 50:50. Structurally, Pd₅₀Cu₅₀ nanoalloys feature a mixed phase consisting of chemically ordered (body-centered cubic type) and disordered (face-centered cubic type) domains. The phase-segregated structure is shown to change to a single phase upon electrochemical potential cycling in ORR condition. While the surface Cu dissolution occurred in PdCu catalysts from the two different synthesis methods, the PdCu with a single-phase character is found to exhibit a tendency of a much greater dissolution than that with the phase segregation. Analysis of the results, along theoretical modeling based on density functional theory calculation, has provided new insights for the correlation between the electrocatalytic activity and the catalyst structures.

KEYWORDS: palladium–copper alloy, nanocatalysts, oxygen reduction reaction, activity–composition synergy, fuel cells, synchrotron X-ray diffraction, atomic pair distribution function



1. INTRODUCTION

To improve the performance of proton exchange membrane fuel cells, alloying noble metals (e.g., Pt, Pd, Au, etc.) with non-noble transition metals (e.g., Co, Ni, Fe, etc.) has been an important focus on the design of advanced catalysts for oxygen reduction reaction (ORR).^{1–5} Currently, Pd-based alloy has attracted increasing attention for preparation of low-cost, highly active, and stable catalysts.^{6–9} For some of the bimetallic alloy nanoparticles (NPs), the enhancement in catalytic activity or selectivity has been attributed to synergistic effect of the surface electronic states on the local strain and effective atomic coordination number.¹⁰ For example, Pd alloyed with transition metals such as nickel (Ni) and copper (Cu) in various bimetallic compositions is being explored in catalytic reactions such as oxygen reduction, alcohol oxidation, and formic acid oxidation reactions.^{11–24} In particular, it has been found that Cu in Pd–Cu nanoalloys plays an important role in the enhancement of the catalytic activity. For example, a recent theoretical study on the catalytic activity of PdCu alloy for ORR indicated that Cu can lower Pd–O binding energy and Pd would increase the Cu–O binding energy in terms of charge

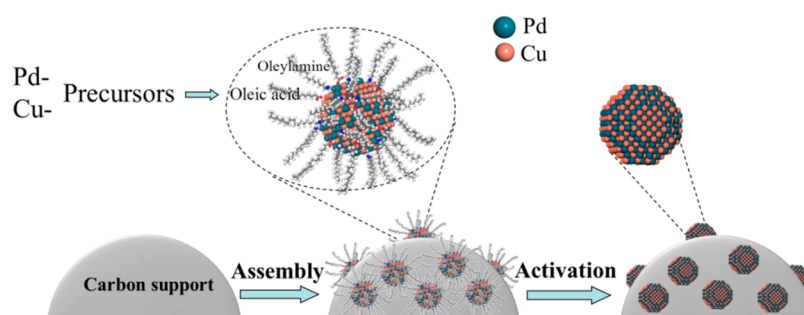
transfer from Cu to Pd with a change in the d band center. Interestingly, Pd–Cu at Pd/Cu ratio of 50:50 is theoretically predicted to be the most active bimetallic composition.¹⁶ There has been however no experimental evidence confirming this prediction. However, thin films of Pd–Cu alloy prepared by sputtering method with different atomic ratios were also predicted theoretically to display a high activity for ORR for Pd₅₀Cu₅₀ in comparison with those of the other bimetallic compositions, which was attributed to an optimal d band shift that makes easier the OOH dissociative adsorption.¹⁷ Notably, different approaches for preparing Pd–Cu alloys show different characteristics in electrocatalysis. Using co-impregnation method to prepare PdCu catalysts with various synthetic molar ratios that were treated under different temperatures, a one-to-one synthetic feeding ratio was shown to exhibit the highest enhancement for ORR activity.¹⁸ Acid treatment was shown to not only dissolve away unalloyed Cu but also remove

Received: September 9, 2015

Accepted: November 5, 2015

Published: November 16, 2015

Scheme 1. Illustration of the Synthesis, Assembly, and Activation of Nanoalloy Particles for the Preparation of the Carbon-Supported Catalysts



a portion of the alloyed Cu. In another study¹⁹ of colloidal preparation of cubic Pd–Cu alloy NPs, the catalysts treated at 500 °C were also shown to display higher ORR activity than those treated at lower temperature, especially for the catalyst prepared by 1:1 synthetic feeding ratio. Similarly, the study on stability of nonporous PdCu alloys with a Pt monolayer as shell shows much stable active surface after 10 000 potential cycles.²⁰ The study of a mixed-PtPd-shell of PtPdCu nanotubes prepared by partially sacrificial Cu nanowires as templates and a voltammetric dealloying process revealed enhanced durability for ORR.²¹ In addition to ORR, Pd–Cu catalysts have also been studied for electrocatalytic oxidation reactions, including formic acid oxidation reaction²² over Pd–Cu/C with 3:1 atomic ratio of Pd and Cu, over core–shell Cu@Pd catalysts with a Pd/Cu atomic ratio of 73:27,²³ and Cu@PdCu/C catalysts that improve the durability and poisoning tolerance for ethanol oxidation reaction.²⁴ Note that most of the previous studies dealt with the bimetallic catalysts based on the synthetic feeding ratios, which are not always the same as those in the resulting bimetallic NPs,^{25,26} especially under the electrocatalysis operation condition.²⁷

Despite these previous studies showing the theoretically predicted high-activity composition of PdCu catalysts and the catalyst activities for catalyst preparation, the question of how exactly the catalytic activity of PdCu nanoalloys is correlated with the exact bimetallic composition in the NPs and atomic-scale structure remains elusive. Recently our study of PdNi nanoalloys revealed how Pd and Ni atoms are rearranged across the alloy NPs upon Ni leaching during electrochemical cycling, and the catalytic activity of the alloys is improved for CO oxidation reaction and ORR,^{26,28} revealing an intriguing composition–activity correlation with the help of high-energy X-ray diffraction (XRD) with atomic pair distribution function (PDF) analysis. The understanding of how such a correlation operates for PdCu nanoalloys could provide further information for assessing the general structural–catalytic synergy of the bimetallic nanoalloy catalysts.

2. EXPERIMENTAL SECTION

Chemicals. Palladium(II) acetylacetonate (Pd(acac)₂, 97%), copper(II) acetylacetonate (Cu(acac)₂, 97%), benzyl ether ((C₆H₅CH₂)₂O, > 98%), ethylene glycol anhydrous (99.8%), oleylamine (CH₃(CH₂)₇CHCH(CH₂)₈NH₂, 70%), 1,2-hexadecanediol (90%), and oleic acid (CH₃(CH₂)₇CH=CH(CH₂)₇COOH, 99+%) were purchased from Aldrich. Other chemicals such as ethanol, hexane, and potassium chlorate were purchased from Fisher Scientific. Vulcan carbon XC-72 was obtained from Cabot. Pd (20% on activated carbon (Pearlman's catalyst), unreduced, 50% water wet paste (Escat 1951, BASF Kit)) was obtained from Strem Chemicals.

Gas of O₂ (20 vol % balanced by N₂) was purchased from Airgas. All chemicals were used as received.

Synthesis of PdCu Nanoparticles and Preparation of the Catalysts. Pd_nCu_{100–n} alloy NPs (*n* represents atomic percentage of Pd in the NPs) were synthesized using two methods.^{29,30} One method involved using benzyl ether (B-) as a solvent to produce PdCu alloy NPs of different compositions (B-PdCu),²⁹ and the other method used ethylene glycol (E-) as a solvent to produce PdCu alloy NPs of different composition (E-PdCu).³⁰ The NPs of different compositions prepared from these two methods are named as B-Pd_nCu_{100–n} and E-Pd_nCu_{100–n} NPs. Briefly, for B-PdCu NPs, palladium(II) acetylacetonate and copper(II) acetylacetonate in a controlled molar ratio were dissolved in benzyl ether solvent. 1,2-Hexadecanediol was added as a reducing agent, and oleic acid and oleylamine were added as a capping agent. Temperature was increased slowly to 105 °C, at which temperature the metal precursors started to decompose and the solution turned dark under N₂ atmosphere. Then the mixture was further heated to 220 °C with reflux for 0.5 h and then cooled to room temperature. NPs were precipitated out by adding ethanol and centrifuging and were then dispersed in hexane solvent for further use. E-PdCu NPs were synthesized similarly except using ethylene glycol as both solvent and reducing agent.³⁰

To prepare carbon-supported NPs, controlled amount of PdCu NPs was mixed with carbon (XC-72) in a hexane solution followed by sonication and overnight stirring. The resulting carbon-supported PdCu NPs, hereafter referred to as PdCu/C NPs (B-PdCu/C and E-PdCu/C), were collected and dried under N₂ atmosphere. The activation of Pd_nCu_{100–n}/C catalysts was achieved by thermochemical processing described elsewhere.^{31–33} Typically, PdCu/C was first treated at 120 °C under N₂ to remove the organic solvent, then kept at 260 °C under O₂ for 1 h to remove the organic capping molecules on the NP surface, and finally calcined at 400 °C under 15 vol % H₂–85% N₂ for 2 h in a programmable furnace. Commercial Pd/C, which was treated at 400 °C under 15 vol % H₂–85% N₂ for 1 h, was used for comparison. The weight loadings were determined by thermogravimetric analysis (TGA) performed on a PerkinElmer Pyris 1-TGA. The general strategy for the synthesis of the nanoalloy particles, the assembly of the particles on a support, and the processing to activate the catalysts is illustrated in Scheme 1.

Morphology, Composition, and Structural Characterization.

Inductively coupled plasma-optical emission spectroscopy (ICP-OES) was used to analyze the chemical composition of the Pd–Cu NPs. The analysis was performed on a PerkinElmer 2000 DV ICP-OES instrument using a Meinhardt nebulizer coupled to a cyclonic spray chamber to increase analyte sensitivity with the following parameters: plasma 18.0 L Ar(g)/min; auxiliary 0.3 L Ar(g)/min; nebulizer 0.63 L Ar(g)/min; power 1500 W; peristaltic pump rate 1.00 mL/min. Laboratory check standards were analyzed for every 6 or 12 samples, with instrument recalibration if the standards were not within ±5% of the initial concentration.

High-angle annular dark-field scanning TEM (HAADF-STEM) was employed to determine the morphology of the PdCu NPs and catalysts. TEM analysis was performed on an FEI Tecnai T12 Spirit Twin TEM/SEM electron microscope (120 kV). Maps of elemental

distribution were obtained by energy dispersive X-ray spectroscopy (EDS). The measurements were performed on a JEOL JEM 2010F with an acceleration voltage of 200 kV and a routine point-to-point resolution of 0.194 nm. The samples were prepared by dropping cast of hexane suspension of NPs onto a carbon-coated copper grid followed by solvent evaporation at room temperature.

Synchrotron high-energy XRD (HE-XRD) experiments aimed at atomic pair distribution functions (PDFs) analysis were performed at Sector 11 of the Advanced Photon Source using X-ray with wavelength of 0.1080 Å. The PdCu/C nanocatalyst samples were loaded into thin-wall glass capillaries with a diameter of 1.5 mm, and XRD data were taken at room temperature in ambient atmosphere. HE-XRD patterns were reduced to the so-called structure factors, $S(q)$, and then Fourier transformed to atomic PDFs $G(r)$. Note atomic PDFs $G(r)$ are experimental quantities that oscillate around zero and show positive peaks at real space distances r , where the local atomic density $\rho(r)$ exceeds the average one ρ_0 . More precisely, by definition, $G(r) = 4\pi r \rho_0 [\rho(r)/\rho_0 - 1]$, where $\rho(r)$ and ρ_0 are the local and average atomic number density, respectively. High-energy XRD and atomic PDFs have already proven to be very efficient in studying the atomic-scale structure of nanosized materials, including metallic alloy NPs.^{34–36}

Electrochemical Measurements. Electrochemical measurements were performed using a microcomputer controlled electrochemical analyzer (CHI600a, CH Instruments). The experiments were performed in three-electrode electrochemical cells with a Pt wire and Ag/AgCl (KCl saturated) electrode as the counter and the reference electrodes, respectively. Glassy carbon (GC) disk coated with a layer of catalysts was used as the working electrode. The GC electrode (geometric area: 0.196 cm²) was polished with 0.005 μm Al₂O₃ powders. The geometric area of the substrate electrode (GC), not the surface area of the catalyst itself, provides a measure of the loading of catalyst on the electrode surface. A typical suspension of the catalysts was prepared by adding 5 mg of catalyst (PdCu/C) to 5 mL of 0.25% Nafion solution and sonicating for 10 min. Then 10 μL of suspension was quantitatively transferred to the surface of the polished GC disk and dried under lamp.

All electrochemical experiments were performed at room temperature, and the electrolytic solution (0.1 M HClO₄) was deaerated with high-purity nitrogen before the cyclic voltammetry (CV) measurements or saturated with oxygen for RDE measurements. Cyclic voltammetry and rotating disk electrode (RDE) measurements were performed after 30 potential cycles between −0.2 and 1.0 V (vs Ag/AgCl (KCl saturated)) in N₂-saturated 0.1 M HClO₄ solution at 50 mV/s to remove contaminant and Cu oxides on the surface and obtain a stable curve.

Computational Modeling. Ab initio calculations were performed by density functional theory (DFT) as implemented in DMol3 program coming as a part of Materials Studio suit programs (Accelrys Inc.).^{37,38} In the calculations, the generalized gradient approximation (GGA) with the Becke–Lee–Yang–Parr (BLYP) exchange correlation functional was used.^{39,40} The localized double numerical basis sets with polarization functions (DNP) were employed for the valence orbitals, and effective core potential was employed to account for the core electrons of metallic species. Full geometry optimizations were performed for all model atomic configurations tested here so that all atoms were fully relaxed. The configurations included unsupported small Pd–Cu clusters. The interactions between the model atomic configurations and O₂ molecule were explored. The energy of adsorption of O₂ on the model atomic configurations was used as a measure of the strength of O₂ adsorption. It was calculated by $E_{\text{ads}} = -(E_{\text{O}_2\text{-metal}} - E_{\text{metal}} - E_{\text{O}_2})$, where, $E_{\text{O}_2\text{-metal}}$, E_{metal} , and E_{O_2} are total energy for the O₂-metal complex, the isolated metal cluster, and the isolated O₂ molecule, respectively.⁴¹

3. RESULTS AND DISCUSSION

Composition and Morphology of PdCu Nanoparticles.

To determine the controllability of the synthesis protocol with respect to the bimetallic composition, the composition of as-

synthesized Pd_nCu_{100−n} NPs was analyzed by ICP-OES. Table 1 shows the composition of as-synthesized B-Pd_nCu_{100−n} NPs (*n*

Table 1. Compositions of as-Synthesized Pd_nCu_{100−n} Nanoparticles Versus Feeding Ratio

PdCu feeding ratio	Pd/Cu ratios in the as-synthesized NPs	
	B-PdCu	E-PdCu
25:75	36:64	25:75
50:50	54:46	58:42
75:25	75:25	77:23

= 36, 54, and 75) and E-Pd_nCu_{100−n} NPs (*n* = 25, 58, and 77) versus the synthetic feeding ratio. The relative amount of Pd in the PdCu NPs increases with the feeding Pd% in the synthesis, showing a close to 1:1 relationship. This finding indicates that the chemical composition of the binary alloy PdCu NPs can be controlled well by controlling the feeding ratio of the metal precursors in the synthesis.

The sizes of as-synthesized B-Pd_nCu_{100−n} NPs are 5.2 ± 1.2, 5.8 ± 1.6, and 4.6 ± 1.1 nm for *n* = 36, 54, and 75, whereas the as-synthesized E-Pd_nCu_{100−n} NPs show smaller sizes, which are 2.7 ± 0.5, 2.6 ± 0.6, and 3.5 ± 0.7 nm for *n* = 25, 58, and 77 (Figure S1, Supporting Information). All the particles appear spherical in shape and relatively uniformly distributed on carbon support. The NPs were examined using HAADF-STEM and EDS, which provided further information for analyzing the detailed morphology and elemental distribution of Pd and Cu atoms in the thermochemically treated carbon-supported NPs. A representative set of results is shown in Figure 1 for carbon-supported B-Pd_nCu_{100−n} (*n* = 36, 54, and 75) NPs. The results show that the thermochemically treated PdCu NPs are mostly crystalline and, importantly, that the Pd and Cu species

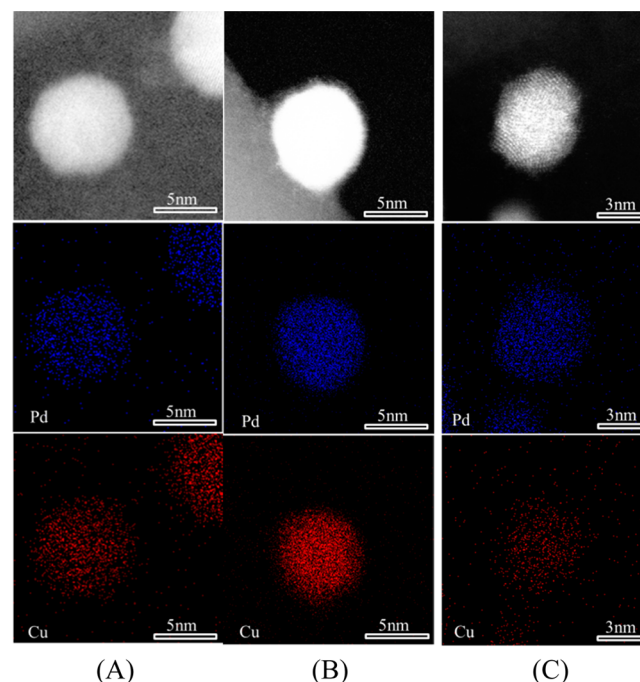


Figure 1. HAADF-STEM images (upper) and elemental maps of Pd and Cu (middle and lower panels) for B-Pd_nCu_{100−n} (*n* = 36 (A), 54 (B), and 75 (C)) NPs (Pd species are in blue, and Cu species are in red).

distribute uniformly across the NPs. This finding is consistent with the alloy characteristic of the PdCu NPs of the different compositions.

The metal loadings of PdCu/C catalysts on the carbon support were determined by TGA. Figure 2 shows a

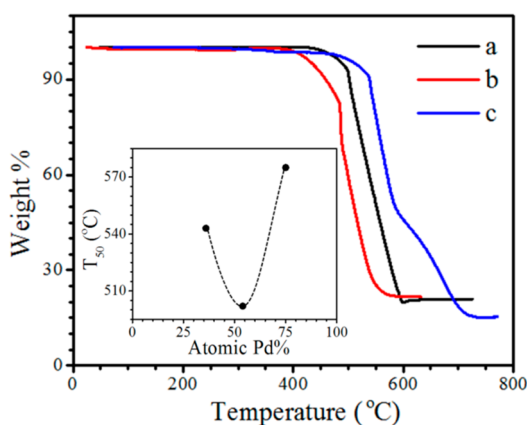


Figure 2. TGA curves for B-Pd_nCu_{100-n}/C ($n = 36$ (a), 54 (b), and 75 (c)) under 30 vol % O₂ at the flow rate of 130 mL/min after thermal treatment (N₂, 120 °C; O₂, 260 °C, 1 h; H₂, 400 °C, 2 h). Inset: Temperature for 50% burning of carbon (T_{50}) vs composition.

representative set of TGA curves for B-Pd_nCu_{100-n}/C catalysts. The loading of the nanoalloy particles was found to be 21, 22, and 15 wt % for $n = 36$, 54, and 75, respectively, after the thermochemical treatment. For E-Pd_nCu_{100-n}/C catalysts, the loading was found to be 12, 13, and 14 wt % for $n = 25$, 58, and 77, respectively. In comparison with the initial estimated loading (~10 wt %), the somewhat increase of the actual loading indicates that the E-PdCu catalyst showed a smaller degree of burning of carbon support than the B-PdCu catalyst after thermal treatment. Interestingly, the burning temperature was found to depend on the bimetallic composition, as shown by the temperature for 50% burning of carbon (T_{50}) versus bimetallic composition in Figure 2, inset. The Pd₅₄Cu₄₆/C catalyst exhibited the lowest T_{50} . This finding suggests that Pd₅₄Cu₄₆/C is possibly the most active catalyst in B-

Pd_nCu_{100-n}/C catalysts for catalytic activation of oxygen species, which will be further evidenced by the ORR activity data in a later section. Note that this trend was not evident for the E-PdCu catalysts, indicating its dependence on the detailed structure of the catalysts.

Phase State of PdCu Alloy Nanoparticles. The phase state of PdCu catalysts was further studied by analysis of the atomic PDFs extracted from HE-XRD patterns, as shown in Figure 3. The detailed phase properties clearly depend on the nanoalloy catalyst preparation methods even with the same thermochemical treatment.⁴² For E-Pd_nCu_{100-n}/C NPs, they feature a single nanophase with chemically disordered ($Fm\bar{3}m$) face-centered cubic (fcc)-type structure. The lattice parameters increase with increasing Pd%. However, the phase state of B-Pd_nCu_{100-n}/C NPs show a rather unique pattern. Specifically, when Cu or Pd species dominate in terms of abundance, as is the case with Pd₃₆Cu₆₄ and Pd₇₅Cu₂₅ NPs, they show a single phase nanoalloy fcc-type structures that are similar to those for E-Pd_nCu_{100-n}/C NPs. However, Pd₅₄Cu₄₆ NPs with Pd and Cu species being almost equal in concentration appear to show phase segregation into a chemically ordered ($Pm\bar{3}m$) body-centered cubic (bcc)-type and chemically disordered ($Fm\bar{3}m$) fcc phases. The two nanophases are distinct in terms of lattice parameters, 2.997 and 3.779 Å, respectively.

Electrocatalytic Activity for Oxygen Reduction Reaction. To understand the composition-dependent synergistic effect on the catalytic activity, which is important for ultimately exploring its application, the carbon-supported Pd_nCu_{100-n} NP catalysts were examined using CV and RDE techniques for measuring their electrocatalytic activities for ORR, including electrochemical active area (ECA), mass activity (MA), and specific activity (SA). Figure 4 shows a typical set of CV and RDE curves for B-Pd_nCu_{100-n}/C ($n = 36$, 54, and 75) catalysts in 0.1 M HClO₄ solution, and the one for E-PdCu/C catalyst is seen in Figure S2, Supporting Information. The voltammetric characteristics in the hydrogen adsorption/desorption region (−0.2 to 0.1 V) and palladium oxidation/reduction peaks (0.3 to 0.5 V) showed significant differences for the different compositions of the catalysts. Pd₅₄Cu₄₆/C catalyst exhibited the largest hydrogen adsorption and Pd-oxide reduction peaks, indicative of the largest ECA value (see Figure 5A). This can be

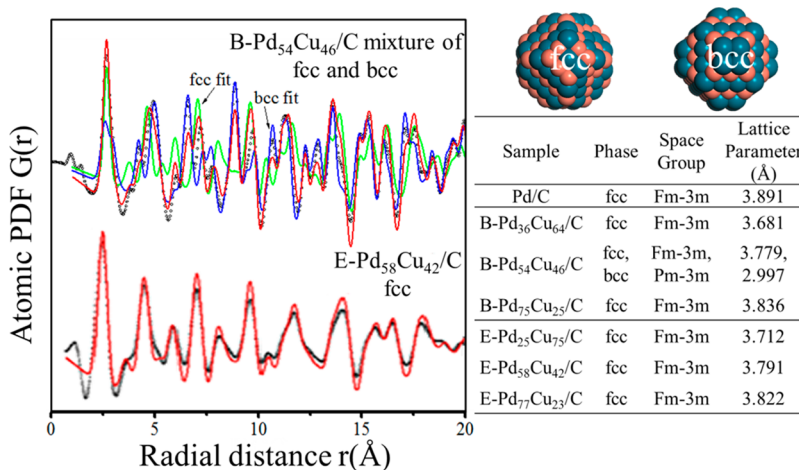


Figure 3. Experimental (symbols) and model-derived (lines) atomic PDFs for B-Pd₅₄Cu₄₆/C and E-Pd₅₈Cu₄₂/C NPs. Lines in red represent the best model approximation to the experimental data. (table) Space group and lattice parameters of the structure models used to approximate the experimental PDFs. The inserted atomic configurations feature fragments of chemically disordered fcc- (space group $Fm\bar{3}m$) and ordered bcc- (space group $Pm\bar{3}m$) type structures. Both have the chemical composition of B-Pd₅₄Cu₄₆/C.

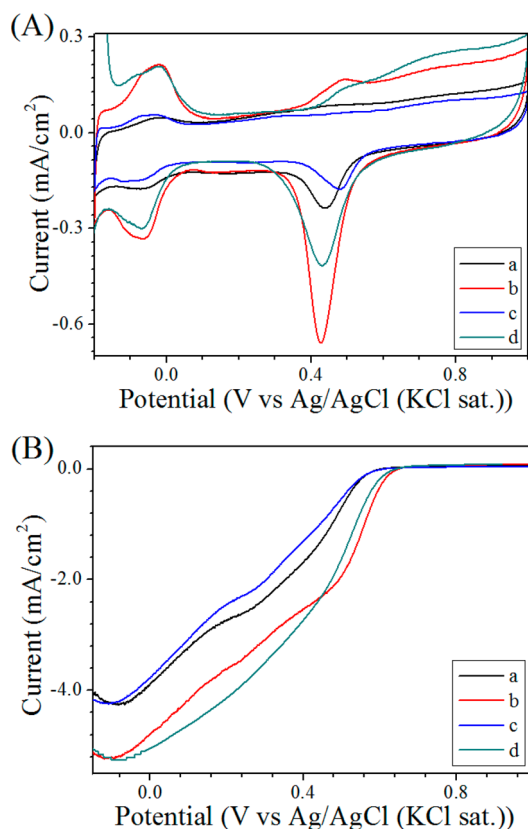


Figure 4. CV (A) and RDE (B) curves for B-Pd_nCu_{100-n}/C ($n = 36$ (a, black), 54 (b, red), 75 (c, blue)), and commercial Pd/C (d, green) catalysts. Electrode: Glassy carbon (0.196 cm²) inked with 10 μg of catalysts; Electrolyte: 0.1 M HClO₄ saturated with N₂ for determining ECA by CV and 0.1 M HClO₄ saturated with O₂ for determining mass activity and specific activity by RDE; scan rate: 50 mV/s (CV), and 10 mV/s and 1600 rpm (RDE).

explained by a greater tendency of surface Cu leaching in Pd₅₄Cu₄₆/C that leads to Pd-enrichment on the surface, producing increased surface sites for hydrogen adsorption. As can be seen from Figure 4B, the RDE curves appear to show two stages of limiting current at ca. -0.1 and 0.3 V, respectively. The current density at Stage 2 is nearly twice that of Stage 1. On the basis of the approximate limiting current measured from the RDE curve, and using Koutecky–Levich equation, the electron transfer number (n) at Stage 2 is determined to be 3.8 (see Supporting Information), a value very close to the expected four-electron reduction for ORR. However, the significant overlapping of the currents in Stages 1 and 2 poses a complication for a precise assessment at this point. It is possible that the ORR possibly proceeds through two paths: a two-electron transfer reaction to produce H₂O₂ and a direct four-electron transfer reaction to produce H₂O.

Considering the differences in Pd loading for different catalysts on the electrode surface, the changes of the kinetic currents with the composition of the NPs are translated to changes in mass activity and specific activity using Koutecky–Levich equation for the comparison of their electrocatalytic activities. Both the mass activity and specific activity data were obtained from the kinetic current at 0.55 V versus Ag/AgCl (KCl saturated). Figure 5 shows a typical set of ECA, mass activity, and specific activity data for B-Pd_nCu_{100-n}/C ($n = 36$, 54, 75) and E-Pd_nCu_{100-n}/C ($n = 25$, 58, 77) catalysts (also see Table S1, Supporting Information). As can be seen from Figure

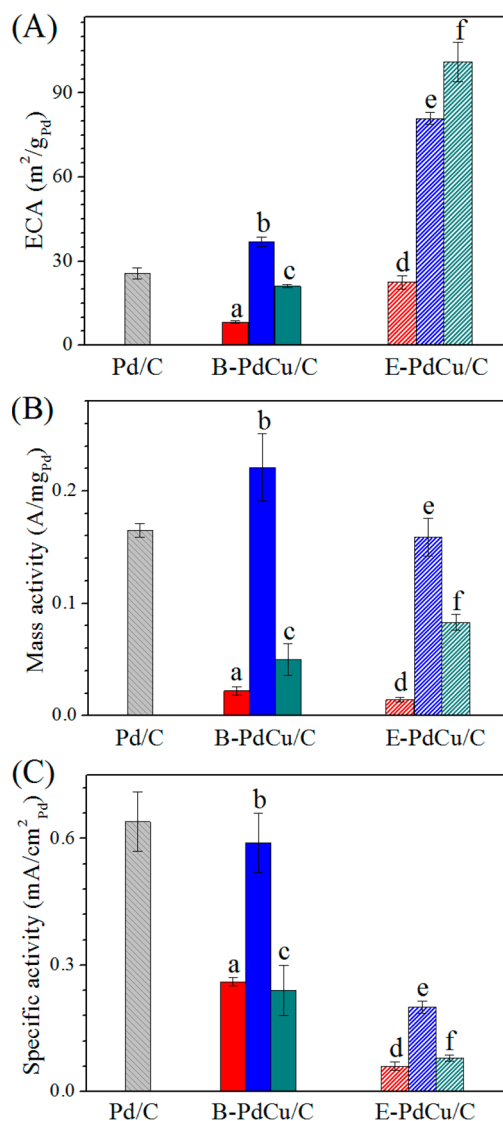


Figure 5. Comparisons of ECAs (A), mass activities (B), and specific activities (C) for B-Pd_nCu_{100-n}/C ($n = 36$ (a), 54 (b), 75 (c)) and E-Pd_nCu_{100-n}/C ($n = 25$ (d), 58 (e), 77 (f)) catalysts. Electrode: Glassy carbon (0.196 cm²) inked with 10 μg of catalysts; Electrolyte: O₂-saturated 0.1 M HClO₄.

5A, E-Pd_nCu_{100-n}/C catalysts clearly show a larger increase of ECA values with increasing Pd% than B-Pd_nCu_{100-n}/C catalysts, exhibiting a maximum value at $n \approx 50$. This finding can be attributed to the smaller NP sizes for E-Pd_nCu_{100-n}/C catalysts, thus producing more hydrogen adsorption sites. Apparently, the mass activity depends on the bimetallic composition, displaying a maximum value at $n \approx 50$ (Figure 5B) for both B-Pd_nCu_{100-n}/C and E-Pd_nCu_{100-n}/C catalysts. A similar trend was also observed for the specific activity (Figure 5C). The observation of the maximum catalytic performance for the catalyst with a Pd/Cu ratio close to 50:50 is in fact consistent with the catalytic burning of the carbon materials as shown in TGA data (see Figure 2). There is clearly a catalytic synergy of Pd and Cu species on the nanoalloy surface. In addition, B-Pd_nCu_{100-n}/C catalyst showed a catalytic activity higher than E-Pd_nCu_{100-n}/C catalyst. This difference is believed to originate from the subtle structural difference as revealed by the HE-XRD/PDF analysis.

Remarkably, a detailed comparison of the electrochemical properties between B-Pd_nCu_{100-n}/C and E-Pd_nCu_{100-n}/C catalysts revealed some subtle differences. Figure 6A shows a

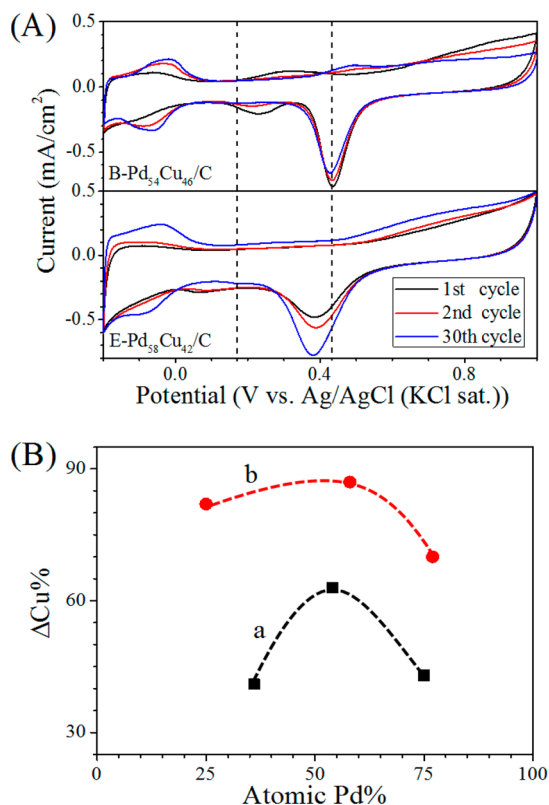


Figure 6. (A) CV curves of B-Pd₅₄Cu₄₆/C (upper) and E-Pd₅₈Cu₄₂/C (lower) at different potential cycles. (B) The loss of Cu ($\Delta\text{Cu}\%$) in B-Pd_nCu_{100-n}/C (a) and E-Pd_nCu_{100-n}/C (b) after extensive (3000) cycles in N₂-saturated 0.1 M HClO₄ solution at 50 mV/s. Calculated assuming Cu is the only leaching species.

representative set of CV curves recorded during the initial potential cycles for B-Pd₅₄Cu₄₆/C and E-Pd₅₈Cu₄₂/C in N₂-saturated 0.1 M HClO₄ solution. For B-Pd₅₄Cu₄₆/C, the first cycle shows a couple of nearly reversible redox peaks between 0.1 and 0.4 V. They are characteristic of Cu species oxidation and Cu oxide reduction, reflecting the existence of phase segregation in the catalyst. In the subsequent cycles, the redox peak currents gradually decreased and disappeared after 30 cycles. The resulting stable CV characteristic is consistent with a decreased degree of phase segregation of the NP catalyst. However, no redox peaks of Cu were observed for E-Pd₅₈Cu₄₂/C catalyst during potential cycling, reflecting its single-phase character, as probed in detail by HE-XRD/PDF studies. In addition, as shown in Figure 6A, the hydrogen adsorption/desorption peaks between -0.2 and 0.1 V increase with the number of cycles for both B-Pd₅₄Cu₄₆/C and E-Pd₅₈Cu₄₂/C, which can be explained by considering the surface Cu dissolution from the NPs, leading to Pd-enrichment on the surface.

To assess the degree of Cu dissolution in the NP catalysts, the changes of composition for B-Pd_nCu_{100-n}/C and E-Pd_nCu_{100-n}/C catalysts were investigated after extensive potential cycling (~ 3000 cycles) between 1.0 and -0.2 V at 100 mV/s in N₂-saturated 0.1 M HClO₄ solution. A typical set of data is shown in Figure 6B (also see Table S2 and Figure S3,

Supporting Information). Clearly, E-Pd_nCu_{100-n}/C catalyst exhibits a more pronounced Cu dissolution ($\Delta\text{Cu}\%$) than B-Pd_nCu_{100-n}/C catalyst. This result indicates that B-Pd_nCu_{100-n}/C catalyst is more stable than E-Pd_nCu_{100-n}/C catalyst, an indication that their structural difference might have played a role in the nanoalloy stability. Moreover, $\Delta\text{Cu}\%$ is shown to reach a maximum at $n \approx 50$ for both B-Pd_nCu_{100-n}/C and E-Pd_nCu_{100-n}/C catalysts.

To aid the assessment of the activity–composition synergy, the fcc lattice parameter is shown in Figure 7. There is clearly a

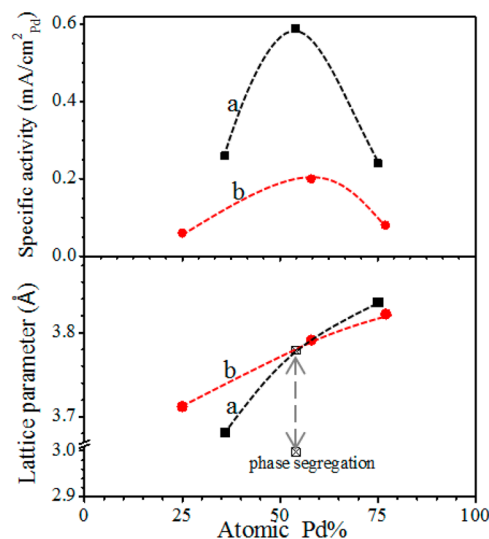


Figure 7. Correlation of specific activities (upper) and the fcc lattice parameter (lower) for B-Pd_nCu_{100-n}/C (a) and E-Pd_nCu_{100-n}/C (b).

correlation between the specific activity and the lattice parameter for B-Pd_nCu_{100-n}/C and E-Pd_nCu_{100-n}/C catalysts. Both catalysts have a similar trend in lattice parameter as a function of the bimetallic composition, that is, increase with increasing Pd%. However, the specific activity shows a maximum at $\sim 50\%$ Pd for both B- and E-Pd_nCu_{100-n}/C catalysts. In comparison with B-PdCu catalysts, the smaller particle size for E-PdCu catalysts exhibits a relatively larger ECA value, leading to a reduction of specific activity due to its inverse proportionality to ECA.

This type of composition-driven enhancement in ORR activity was also supported by the result from a DFT calculation based on small Pd–Cu cluster models. While the limited number of atoms in the model clusters oversimplified the nanoalloy structures, it provides some useful information for understanding why Pd₅₀Cu₅₀ composition has a higher catalytic activity than the other bimetallic compositions. In the DFT calculation, molecular chemisorption of O₂ on each of the model clusters (Pd₁₃, Pd₁₀Cu₃, Pd₆Cu₇, and Pd₃Cu₁₀) was modeled mainly using bridge type (see Table S3, Supporting Information).⁴³

The resulting oxygen adsorption energy (see Figure 8) revealed an intermediate value for Pd₆Cu₇. However, the increase of Pd–O bond distance with increasing Cu content in the model clusters shows a relatively larger value for Pd₆Cu₇. In addition, the length of O–O bond (Table S3 and Figure S4, Supporting Information) was found to remain largely the same except Pd₃Cu₁₀. To a certain extent, the preliminary DFT modeling results are supportive of the presence of a maximum ORR activity at $n \approx 50$ for the Pd_nCu_{100-n} catalysts.

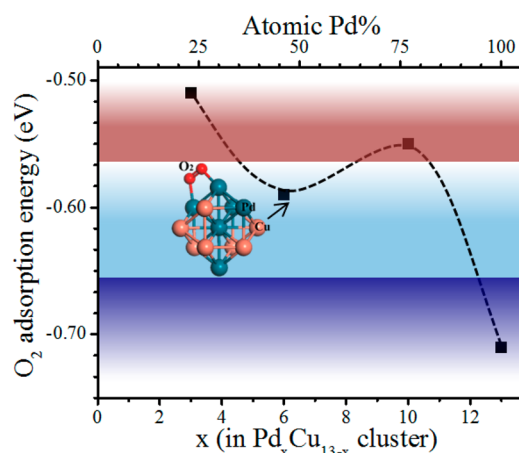


Figure 8. Adsorption energy for molecularly adsorbed O_2 on Pd_xCu_{13-x} cluster obtained by DFT.

Our findings have provided a clear piece of experimental evidence confirming the theoretical prediction of the maximized catalytic activity for Pd_nCu_{100-n}/C catalysts with a Pd/Cu ratio of $\sim 50:50$.¹⁵ This synergy is consistent with the assessment that Cu can lower Pd–O binding energy and that Pd would increase the Cu–O binding energy in terms of charge transfer from Cu to Pd, leading to an optimal shift in the d-band center to an intermediate position for the catalyst with a ratio of Pd/Cu $\approx 50:50$.¹⁶ This was explained by decreasing Pd's d-band upon adding Cu, whereas increasing Cu's d-band upon adding Pd in the alloy. Such a d-band shift would favor an intermediate adsorption energy of oxygen on the Pd/Cu $\approx 50:50$ catalyst, leading to an enhanced catalytic activity.

4. CONCLUSION

Taken together, the results from the structural and electrochemical characterizations of Pd_nCu_{100-n}/C catalysts for ORR have revealed a synergistic correlation between the catalytic activity, atomic-scale structure and composition of the catalysts. Depending on the catalyst preparation method, the $Pd_{50}Cu_{50}/C$ catalyst is either a single, fcc-type phase or phase-segregated into domains of chemically ordered bcc- and chemically disordered fcc-type structure. The lattice parameter of the Pd_nCu_{100-n}/C catalysts was shown to increase with increasing Pd%, with the alloy character remaining unchanged after thermochemical treatment. A maximum ORR activity was observed for a catalyst with the Pd/Cu ratio close to 50:50. This catalyst is shown to change to a single phase upon potential cycling in the ORR condition. With potential cycling, the surface dissolution of Cu from the PdCu catalysts is also shown to depend on the catalyst phase state and composition. The results have provided new insights into the structure–composition activity synergy, which is important for the design of nanoalloy catalysts with tunable catalytic properties. Note that this work has focused on the catalytic properties of the catalysts in acidic electrolytes; a further study of the catalytic properties in different electrolytes, especially in alkaline electrolytes, where the surface reactivity of the nanoalloy catalysts is very different from that in the acidic electrolyte, should provide additional insight into the structure–composition–activity synergy. This is part of our future work.

■ ASSOCIATED CONTENT

Supporting Information

The Supporting Information is available free of charge on the ACS Publications website at DOI: 10.1021/acsami.5b08478.

High-angle annular dark field scanning HAADF-STEM images, CV and RDE curves, comparison of ECA, mass activity, and specific activity, tabulated bond distances, illustrated catalysts, plot of calculated Pd–O bond length, discussion of calculation of number of electrons, additional references. (PDF)

■ AUTHOR INFORMATION

Corresponding Author

*E-mail: cjzhong@binghamton.edu.

Notes

The authors declare no competing financial interest.

■ ACKNOWLEDGMENTS

This work was supported by the DOE-BES Grant DE-SC0006877. Work at the Advanced Photon Source was supported by DOE under Contract No. DE-AC02-06CH11357. J.W. acknowledges a scholarship support from CSC.

■ REFERENCES

- (1) You, D. J.; Jin, S.; Lee, K. H.; Pak, C.; Choi, K. H.; Chang, H. Improvement of activity for oxygen reduction reaction by decoration of Ir on PdCu/C catalyst. *Catal. Today* **2012**, *185*, 138–142.
- (2) Luo, J.; Yin, J.; Loukrakpam, R.; Wanjala, B. N.; Fang, B.; Shan, S.; Yang, L.; Ng, M. S.; Kinzler, J.; Kim, Y.-S.; Zhong, C. J.; Nie, M.; Luo, K. K. Design and Characterization of Ternary Alloy Electrocatalysts for Oxygen Reduction Reaction. *J. Electroanal. Chem.* **2013**, *688*, 196–206.
- (3) Li, B.; Prakash, J. Oxygen reduction reaction on carbon supported Palladium-Nickel alloys in alkaline media. *Electrochem. Commun.* **2009**, *11*, 1162–1165.
- (4) Wanjala, B.; Fang, B.; Loukrakpam, R.; Chen, Y.; Engelhard, M.; Luo, J.; Yin, J.; Yang, L.; Shan, S.; Zhong, C. J. Role of Metal Coordination Structures in Enhancement of Electrocatalytic Activity of Ternary Nanoalloys for Oxygen Reduction Reaction. *ACS Catal.* **2012**, *2*, 795–806.
- (5) Shen, S. Y.; Zhao, T. S.; Xu, J. B.; Li, Y. S. Synthesis of PdNi catalysts for the oxidation of ethanol in alkaline direct ethanol fuel cells. *J. Power Sources* **2010**, *195*, 1001–1006.
- (6) Shao, M. H.; Liu, P.; Zhang, J. L.; Adzic, R. R. Origin of Enhanced Activity in Palladium Alloy Electrocatalysts for Oxygen Reduction Reaction. *J. Phys. Chem. B* **2007**, *111*, 6772–6775.
- (7) Shao, M. H. Palladium-based electrocatalysts for hydrogen oxidation and oxygen reduction reactions. *J. Power Sources* **2011**, *196*, 2433–2444.
- (8) Grden, M.; Lukaszewski, M.; Jerkiewicz, G.; Czerwinski, A. Electrochemical behaviour of palladium electrode: Oxidation, electro-dissolution and ionic adsorption. *Electrochim. Acta* **2008**, *53*, 7583–7598.
- (9) Zhao, J.; Sarkar, A.; Manthiram, A. Synthesis and characterization of Pd-Ni nanoalloy electrocatalysts for oxygen reduction reaction in fuel cells. *Electrochim. Acta* **2010**, *55*, 1756–1765.
- (10) Singh, A. K.; Xu, Q. synergistic catalysis over bimetallic alloy nanoparticles. *ChemCatChem* **2013**, *5*, 652–676.
- (11) Kuttiyiel, K. A.; Sasaki, K.; Su, D.; Vukmirovic, M. B.; Marinkovic, N. S.; Adzic, R. R. Pt monolayer on Au-stabilized PdNi core-shell nanoparticles for oxygen reduction reaction. *Electrochim. Acta* **2013**, *110*, 267–272.
- (12) Filhol, J. S.; Simon, D.; Sautet, P. Understanding the High Activity of a Nanostructured Catalyst Obtained by a Deposit of Pd on

Ni: First Principle Calculations. *J. Am. Chem. Soc.* **2004**, *126*, 3228–3233.

(13) Du, C. Y.; Chen, M.; Wang, W. G.; Yin, G. P. Nanoporous PdNi Alloy Nanowires As Highly Active Catalysts for the Electro-Oxidation of Formic Acid. *ACS Appl. Mater. Interfaces* **2011**, *3*, 105–109.

(14) Qi, Z.; Geng, H. R.; Wang, X. G.; Zhao, C. C.; Ji, H.; Zhang, C.; Xu, J. L.; Zhang, Z. G. Novel nanocrystalline PdNi alloy catalyst for methanol and ethanol electro-oxidation in alkaline media. *J. Power Sources* **2011**, *196*, 5823–5828.

(15) Zhang, H.; Hao, Q.; Geng, H. R.; Xu, C. X. Nanoporous PdCu alloys as highly active and methanol-tolerant oxygen reduction electrocatalysts. *Int. J. Hydrogen Energy* **2013**, *38*, 10029–10038.

(16) Tang, W. J.; Zhang, L.; Henkelman, G. Catalytic Activity of Pd/Cu Random Alloy Nanoparticles for Oxygen Reduction. *J. Phys. Chem. Lett.* **2011**, *2*, 1328–1331.

(17) Fouda-Onana, F.; Bah, S.; Savadogo, O. Palladium–copper alloys as catalysts for the oxygen reduction reaction in an acidic media I: Correlation between the ORR kinetic parameters and intrinsic physical properties of the alloys. *J. Electroanal. Chem.* **2009**, *636*, 1–9.

(18) Wang, X. P.; Kariuki, N.; Vaughey, J. T.; Goodpaster, J.; Kumar, R.; Myers, D. J. Bimetallic Pd–Cu Oxygen Reduction Electrocatalysts. *J. Electrochem. Soc.* **2008**, *155*, 602–609.

(19) Kariuki, N. N.; Wang, X. P.; Mawdsley, J. R.; Ferrandon, M. S.; Niyogi, S. G.; Vaughey, J. T.; Myers, D. J. Colloidal Synthesis and Characterization of Carbon-Supported Pd–Cu Nanoparticle Oxygen Reduction Electrocatalysts. *Chem. Mater.* **2010**, *22*, 4144–4152.

(20) Hou, L. X.; Qiu, H. J. Enhanced electrocatalytic performance of Pt monolayer on nanoporous PdCu alloy for oxygen reduction. *J. Power Sources* **2012**, *216*, 28–32.

(21) Li, H. H.; Cui, C. H.; Zhao, S.; Yao, H. B.; Gao, M. R.; Fan, F. J.; Yu, S. H. Mixed-PtPd-Shell PtPdCu Nanoparticle Nanotubes Templated from Copper Nanowires as Efficient and Highly Durable Electrocatalysts. *Adv. Energy Mater.* **2012**, *2*, 1182–1187.

(22) Lu, L.; Shen, L. P.; Shi, Y.; Chen, T. T.; Jiang, G. Q.; Ge, C. W.; Tang, Y. W.; Chen, Y.; Lu, T. H. New insights into enhanced electrocatalytic performance of carbon supported Pd–Cu catalyst for formic acid oxidation. *Electrochim. Acta* **2012**, *85*, 187–194.

(23) Ren, M. J.; Zhou, Y.; Tao, F. F.; Zou, Z. Q.; Akins, D. L.; Yang, H. Controllable Modification of the Electronic Structure of Carbon-Supported Core–Shell Cu@Pd Catalysts for Formic Acid Oxidation. *J. Phys. Chem. C* **2014**, *118*, 12669–12675.

(24) Cai, J. D.; Zeng, Y. Z.; Guo, Y. L. Copper@palladiumcopper core-shell nanospheres as a highly effective electrocatalyst for ethanol electro-oxidation in alkaline media. *J. Power Sources* **2014**, *270*, 257–261.

(25) Loukrakpam, R.; Shan, S.; Petkov, V.; Yang, L.; Luo, J.; Zhong, C. J. Atomic Ordering Enhanced Electrocatalytic Activity of Nanoalloys for Oxygen Reduction Reaction. *J. Phys. Chem. C* **2013**, *117*, 20715–20721.

(26) Wu, J. F.; Shan, S. Y.; Petkov, V.; Prasai, B.; Cronk, H.; Joseph, P.; Luo, J.; Zhong, C. J. Composition-Structure-Activity Relationships for Palladium-Alloyed Nanocatalysts in Oxygen Reduction Reaction: An Ex-Situ/In-Situ High Energy X-ray Diffraction Study. *ACS Catal.* **2015**, *5*, 5317–5327.

(27) Shan, S.; Luo, J.; Wu, J.; Kang, N.; Zhao, W.; Cronk, H.; Zhao, Y.; Joseph, P.; Petkov, V.; Zhong, C. J. Nanoalloy Catalysts for Electrochemical Energy Conversion and Storage Reactions. *RSC Adv.* **2014**, *4*, 42654–42669.

(28) Shan, S.; Petkov, V.; Yang, L.; Luo, J.; Joseph, P.; Mayzel, D.; Prasai, B.; Wang, L.; Engelhard, M.; Zhong, C. J. Atomic-Structural Synergy for Catalytic CO Oxidation over Palladium-Nickel Nanoalloys. *J. Am. Chem. Soc.* **2014**, *136*, 7140–7151.

(29) Yin, Z.; Zhou, W.; Gao, Y. J.; Ma, D.; Kiely, C. J.; Bao, X. H. Supported Pd–Cu Bimetallic Nanoparticles That Have High Activity for the Electrochemical Oxidation of Methanol. *Chem. - Eur. J.* **2012**, *18*, 4887–4893.

(30) Yin, J.; Shan, S.; Ng, M. S.; Yang, L. F.; Mott, D.; Fang, W.; Kang, N.; Luo, J.; Zhong, C. J. Catalytic and Electrocatalytic Oxidation

of Ethanol over Palladium-Based Nanoalloy Catalysts. *Langmuir* **2013**, *29*, 9249–9258.

(31) Shan, S. Y.; Petkov, V.; Yang, L. F.; Mott, D.; Wanjala, B. N.; Cai, F.; Chen, B. H.; Luo, J.; Zhong, C. J. Oxophilicity and Structural Integrity in Maneuvering Surface Oxygenated Species on Nanoalloys in CO Oxidation. *ACS Catal.* **2013**, *3*, 3075–3085.

(32) Mukundan, V.; Yin, J.; Joseph, P.; Luo, J.; Shan, S.; Zakharov, D. N.; Zhong, C. J.; Malis, O. Nanoalloying and phase transformations during thermal treatment of physical mixtures of Pd and Cu nanoparticles. *Sci. Technol. Adv. Mater.* **2014**, *15*, 025002.

(33) Yang, L.; Shan, S.; Loukrakpam, R.; Petkov, V.; Ren, Y.; Wanjala, B.; Engelhard, M.; Luo, J.; Yin, J.; Chen, Y.; Zhong, C. J. Role of support-nanoalloy interactions in the atomic-scale structural and chemical ordering for tuning catalytic sites. *J. Am. Chem. Soc.* **2012**, *134*, 15048–15060.

(34) Petkov, V. Nanostructure by high-energy X-ray diffraction. *Mater. Today* **2008**, *11*, 28–38.

(35) Egami, T.; Billinge, S. J. L. *Underneath the Bragg's Peak: structural analysis of complex materials*; Pergamon: Amsterdam, 2003.

(36) Oxford, S. M.; Lee, P. L.; Chupas, P. J.; Chapman, K. W.; Kung, M. C.; Kung, H. H. Study of Supported PtCu and PdAu Bimetallic Nanoparticles Using In-Situ X-ray Tools. *J. Phys. Chem. C* **2010**, *114*, 17085–17091.

(37) Xia, M. R.; Ding, W.; Xiong, K.; Li, L.; Qi, X. Q.; Chen, S. G.; Hu, B. S.; Wei, Z. D. Anchoring Effect of Exfoliated-Montmorillonite-Supported Pd Catalyst for the Oxygen Reduction Reaction. *J. Phys. Chem. C* **2013**, *117*, 10581–10588.

(38) Chang, C. R.; Wang, Y. G.; Li, J. Theoretical Investigations of the Catalytic Role of Water in Propene Epoxidation on Gold Nanoclusters: A Hydroperoxyl-Mediated Pathway. *Nano Res.* **2011**, *4*, 131–142.

(39) Wang, L.; Wang, Y.; Song, S. Q.; Shen, P. K. Density functional theory study on the mechanism for enhanced activity of Pd_xNi/C catalysts. *Chin. J. Catalysis* **2009**, *30*, 433–439.

(40) Tang, W. J.; Zhang, L.; Henkelman, G. J. Catalytic activity of Pd/Cu random alloy nanoparticles for oxygen reduction. *J. Phys. Chem. Lett.* **2011**, *2*, 1328–1331.

(41) Chang, C. R.; Wang, Y. G.; Li, J. Theoretical Investigations of the Catalytic Role of Water in Propene Epoxidation on Gold Nanoclusters: A Hydroperoxyl-Mediated Pathway. *Nano Res.* **2011**, *4*, 131–142.

(42) Shan, S. Y.; Petkov, V.; Prasai, B.; Wu, J. F.; Joseph, P.; Skeete, Z.; Kim, E.; Mott, D.; Malis, O.; Luo, J.; Zhong, C. J. Catalytic activity of bimetallic catalysts highly sensitive to the atomic composition and phase structure at the nanoscale. *Nanoscale* **2015**, DOI: 10.1039/C5NR04535E.

(43) Wang, L.; Williams, J. I.; Lin, T.; Zhong, C. J. Spontaneous reduction of O₂ on PtVFe nanocatalysts. *Catal. Today* **2011**, *165*, 150–159.